

Multi-Resolution Radiative Transfer for Line Emission

M. Juvela

Helsinki University Observatory, Tähtitorninmäki, P.O.Box 14, SF-00014 University of Helsinki, Finland

`mika.juvela@helsinki.fi`

and

P. Padoan

University of California, San Diego

ABSTRACT

Radiative transfer calculations are crucial for modelling interstellar clouds because they provide the link between physical conditions in a cloud and the radiation observed from it. Three-dimensional simulations of magnetohydrodynamic (MHD) turbulence are used to study the structure and dynamics of interstellar clouds and even to follow the initial stages of core collapse leading to the formation of new stars. The wide range of size scales in such models poses a serious challenge to radiative transfer calculations.

In this paper we describe a new computer code that solves the radiative transfer problem on multi-resolution grids. If the cloud model is from an MHD simulation on a regular cartesian grid, criteria based for example on local density or velocity gradients are used to refine the grid by dividing selected cells into sub-cells. Division can be repeated hierarchically. Alternatively, if the cloud model is from an MHD simulations with adaptive mesh refinement, the same multi-resolution grid used for the MHD simulation is adopted in the radiative transfer calculations. High discretization is often needed only in a small fraction of the total volume. This makes it possible to simulate spectral line maps with good accuracy, also minimizing the total number of cells and the computational cost (time and memory).

Multi-resolution models are compared with models on regular grids. In the case of moderate optical depths (e.g. $\tau \sim$ a few) an accuracy of 10% can be reached with multi-resolution models where only 10% of the cells of the full grid are used. For optically thick species ($\tau \sim 100$), the same accuracy is achieved using 15% of the cells. The relation between accuracy and number of cells is

not found to be significantly different in the two MHD models we have studied. The new code is used to study differences between LTE and non-LTE spectra and between isothermal and non-isothermal cloud models. We find significant differences in line ratios and individual spectral line profiles of the isothermal and LTE models relative to the more realistic non-isothermal case. The slope of the power spectrum of integrated intensity is instead very similar in all models.

Subject headings: ISM: clouds – Radiative transfer – Radio lines: ISM

1. Introduction

Radiative transfer calculations in three dimensions allow us to study the effects of density inhomogeneity and complex velocity fields in interstellar clouds. The first three-dimensional radiative transfer calculations made use of non-physical models of the density and velocity fields (Park & Hong 1995; Park et al. 1996; Juvola 1997; Pagani 1998). A physical description of interstellar cloud structure and kinematics is provided by three-dimensional simulations of magneto-hydrodynamic (MHD) turbulence. Such simulations can presently be run routinely on uniform cartesian grids with up to 512^3 computational cells (e.g. Li, Norman, Mordecai 2004) and on multi-resolution grids with adaptive mesh refinement (AMR) methods yielding a spatial resolution of many orders of magnitude locally (Abel, Bryan & Norman 2002).

Radiative transfer calculations on a single snapshot of an MHD simulation are fast compared with the full MHD simulation and are used for comparison with observational data. However, each MHD solution can be used for a number of radiative transfer runs. Radiative transfer can be solved for different molecular or atomic species and MHD simulations can be scaled to represent clouds of different size, density, and temperature. In view of the possibly large number of radiative transfer calculations based on a single MHD snapshot, the speed of line transfer calculations is important.

Radiative transfer calculations of molecular lines are often based on Monte Carlo methods (Bernes 1979; Choi et al. 1995; Park & Hong 1995; Juvola 1997; Hartstein & Liseau 1998). Monte Carlo methods have the advantage of being simple to implement and easily adaptable to different geometries and spatial discretization. Such flexibility can be important in three-dimensional models where suitable discretization (e.g. partial cylindrical symmetry) can significantly reduce run times. So far most three-dimensional calculations have been carried out on regular cartesian grids. One drawback of Monte Carlo methods is that, due to the random sampling, higher accuracy is obtained only with a large increase in computational cost. Furthermore, the whole model is usually kept in main memory because each of the

randomly generated photons can hit any cell in the model. Finally, it is difficult to carry out Monte Carlo simulations effectively on parallel computers. The lambda operator, Λ , is at the heart of the radiative transfer problem. It maps the source function, S , to the average local intensity of the radiation field, J . In Monte Carlo simulation this is accomplished by simulating model photons and the Λ operator is not used explicitly.

In accelerated lambda iteration (ALI) methods the Λ operator is split into two parts:

$$J = \Lambda S = [(\Lambda - \Lambda^*) + \Lambda^*]S . \quad (1)$$

The operator Λ^* is typically diagonal and represents the contribution of a cell to the radiation field within the same cell (e.g. Scharmer 1981; Rybicki & Hummer 1991, 1992). Iterations are needed to solve for large scale interactions. The convergence of such iterations becomes faster for increasingly higher optical depths and weaker coupling between cells. ALI methods have been used also with two-dimensional (e.g. Auer et al. 1994; Dullemond & Turolla 2000) and three-dimensional grids.

In contrast with Monte Carlo methods, in ALI implementations the sampling of the radiation field is usually not random and is based on a fixed set of characteristics. A characteristic is a line along which the radiative transfer equation is solved and where the intensity of the incoming radiation is known. For long characteristics, integration is done for each cell separately starting from the cloud surface. However, most three-dimensional implementations are based on short characteristics (Kunasz & Auer 1988; Auer & Paletou 1994; Auer et al. 1994). Short characteristics extend only from one cell to the next one and, on cartesian grids, intensity for any given direction may be propagated only one cell layer at a time. This helps reduce memory requirements by dividing the model cloud into separate layers that are treated sequentially. The computational overhead resulting from such division is much smaller than the equivalent overhead in Monte Carlo methods.

The only real difference between Monte Carlo and ALI methods is in the sampling of the radiation field. The so-called accelerated Monte Carlo methods correspond directly to ALI methods (Juvela & Padoan 1999; Hogerheijde & van der Tak 2000; van Zadelhoff et al. 2002). The basic idea in the core saturation method of Hartstein & Liseau (1998) is similar, but uses a distinction between optically thick line centre and optically thin wings.

Computer resources limit the detail of current models. One way to speed up the solution of the radiative transfer problem is to resort to approximations. For example, Ossenkopf (2002) combined a local large velocity gradient (LVG) approximation with an approximation of an isotropic large scale field. Tests with isothermal, three dimensional MHD models showed the accuracy of the method to be $\sim 20\%$ or better while speed-ups were very significant.

Another possibility is to solve the radiative transfer problem without approximations and to decrease the number of cells in the model. Interstellar clouds are very inhomogeneous and volume filling factors derived from molecular line or infrared emission are low, varying from a few tenths in star forming cores (Snell et al. 1984; Creaves et al. 1992) to less than one percent in molecular cloud complexes (Falgarone & Phillips 1991). This suggests the emission of many molecular species can be predicted with high precision even if high spatial resolution is only used for some small fraction of the total volume. Multi-resolution grids are already used in cosmology (Abel, Bryan & Norman 2002), in studies of supernovae driven galactic disk fountains (de Avillez & Berry 2001), to simulate star-forming clouds (Klein et al. 2003) and in studies of incompressible MHD flows (Grauer et al. 2000) thanks to adaptive mesh refinement (AMR) methods. Radiative transfer calculations based on solutions of AMR simulations of MHD turbulence in interstellar clouds must be performed in a way that takes advantage of multi-resolution grids.

In this paper we present a computer code that can be used to solve the radiative transfer problem for line radiation using hierarchically refined spatial discretization. The implementation is presented in Sect. 2. We compute ^{13}CO and ^{12}CO spectra for isothermal models, based on the solution of MHD simulations performed on a regularly spaced cartesian grid. In Sect. 3 we study the accuracy and the reduction in the required computational resources of this multi-resolution code. In Sect. 4 we use the new code to study differences between LTE and non-LTE spectra and between isothermal and non-isothermal cloud models. In Sect. 5 e.g. further improvements to the current code are discussed.

2. The code

2.1. Background: long and short characteristics

The lambda operator Λ can be implemented numerically in different ways, depending on how the intensity averaged over the whole solid angle is computed at each position in the cloud. The simplest way is to use long characteristics (LC) that extend directly from the cloud surface to a grid point inside the cloud (see Fig. 1). The radiative transfer equation is integrated along a LC giving the intensity in one direction. The angle-averaged intensity is then obtained by repeating the calculations for a sufficiently large number of LCs pointing in different directions. These calculations are repeated independently for each grid position.

Calculations with LCs contain redundancy. A LC is used only to estimate intensity at its end point and not for any of the other cells it may cross. In short-characteristic (SC) methods this redundancy is removed. A short characteristic extends only between two

layers of grid points. The grid must be swept in an ordered fashion so that intensities are always known for the previous layer. When a short characteristic is formed and extended backward it usually ends up between grid points in the previous layer. Therefore, intensity at the starting position is first interpolated and integration along the SC then propagates the intensity information to the next layer (see Fig. 1).

In the case of SCs, consecutive interpolations lead to diffusion, that is the intensity propagates not only in the direction of the SCs, but also perpendicular to that. The accuracy of the interpolation is essential to minimize this effect. Auer & Paletou (1994) note that one should use at least second order schemes and additionally guard against negative values introduced by interpolation.

2.2. The basic scheme

In our scheme each grid position represents the centre of a cubic cell and we combine the use of long and short characteristics (see Fig. 2). At any given time only intensities for one cell layer are kept in memory. LCs are initially created at intervals corresponding to the cell size. The intensity is propagated along these LCs. The computation proceeds one layer at a time in order to avoid any redundancy. In order to determine the intensity at the cell centre, a short characteristic is formed. At the starting point of a SC the intensity is linearly interpolated using the values at the positions of the three closest LCs.

Intensities along LCs are the result of direct integration along these lines. This prevents the appearance of any cumulative errors since intensity values do not depend on any interpolation. Interpolation is performed only at the starting position of each SC. The three closest LCs surrounding the SC are selected (see Fig. 2b) and intensity at the start of the SC is obtained with linear interpolation. This operation is much less critical than in pure SC schemes where interpolation would affect all intensities in the downstream direction. In our case interpolation errors are not propagated beyond the current cell. One could even take the intensity of the closest LC without any interpolation. Resulting errors would still correspond only to differences in the radiation field at scales below the size of an individual cell. In integration along SC, the intensity is split into an external part and a part caused by the cell in question, thus leading to an ALI method with a diagonal operator Λ^* .

Previous SC codes were designed to give good accuracy in the case of smoothly varying source functions. For fractal interstellar clouds the underlying density distribution is not smooth and there are no guarantees of accuracy of high order interpolation. We use only linear interpolation when intensities at the starting positions of the SCs are derived. This

is possible since we use LCs to carry intensity information through the whole cloud. We take a simple approach also regarding the integration along the characteristics. As in the Monte Carlo code, we assume the source function and the optical depth are constant within individual cells.

Our code handles three dimensional clouds where basic discretization is done according to a cartesian grid. The program is optimized for low memory requirement so that at any given time only data for one layer of cells are kept in memory. These data include intensities at the positions where LCs enter the current layer of cells. The intensity is interpolated to the starting position of a SC and the integration along the SC gives the intensity at the cell centre. These intensities can be saved to an external file or, if the model size allows it, they can be directly added to counters that are later used to calculate intensities averaged over solid angle. Once LCs have been integrated to the boundary of the next cell layer, data for the previous layer can be removed and data for the next layer are read from external files. This is repeated until all cell layers have been processed. Calculations are repeated for a number of directions. Finally, angle-averaged intensities are computed for each cell. These steps are carried out for each transition separately. It would be more efficient to calculate all transitions simultaneously, but that would also increase the memory requirement by a factor equal to the number of transitions simulated. Once intensities in the cells are known, new estimates of level populations can be computed from the equilibrium equations. Updated source functions and optical depths are then computed and the whole procedure is repeated until changes in the level populations between consecutive iterations are below the required accuracy.

2.3. Hierarchical refinement

A multi-resolution model cloud may be directly provided as the solution of an AMR simulation of MHD turbulence. If the model cloud is instead the solution of the MHD equations on a regular cartesian grid, a multi-resolution grid can be obtained prior to the radiative transfer calculations. We refer to the lowest resolution root grid as the level 1 grid. At the level 1, each cell can be divided into eight level 2 cells and this division can be repeated for any of the sub-cells. High levels of discretization are used in regions where high accuracy is required to compute the spectral line maps, such as in regions of high density or large velocity gradients. The specific refinement criterion can be fit to the specific model and needs.

The method described in the previous chapter is used to calculate the intensities in the multi-resolution models. Because the code is designed to minimize the memory requirement,

only one layer of level 1 cells and their possible sub-cells are kept in memory. For each cell touching the upper boundary of the layer there should be exactly one LC. Cells at level 1 are handled row by row starting with the upstream direction as defined by the orientation of the LCs. Within each level 1 cell all sub-cells and the corresponding LCs are processed recursively in the same order. Each LC is integrated down to the next boundary between level 1 cells. After these calculations intensities are known in each position where a LC hits a new cell and later these values are interpolated to give intensities at the start positions of the SCs.

In multi-resolution models new LCs are created or destroyed as discretization changes (Fig. 3). If a LC enters a smaller cell, new LCs must be created, one for each of the neighbouring sub-cells. Three new LCs must be created if change is from level 1 to level 2 (or from level 2 to 3); 15 if change is directly from level 1 to level 3. Intensities for the new LCs are interpolated between the nearest existing LCs. A more simple procedure would be to copy the intensities from the nearest LC and errors would again correspond only to intensity variations at distances smaller than the size of the cell from which the LC come. Currently this procedure is used only when interpolation is not possible, for positions without suitable LCs on opposite sides (see Fig. 3).

When a LC comes from a smaller cell into a larger cell it may have to be removed. For this purpose, a level number is attached to each LC. For example, if a LC is created entering a level l cell, it will be destroyed only when it enters a cell with level smaller than l . When some of level l LCs are destroyed one could calculate the average of the remaining LCs at level $l - 1$. Currently unnecessary LCs are only deleted and the remaining LC at level $l - 1$ represents the intensity integrated strictly along that one line-of-sight.

The implementation of the program is discussed further in Appendix A.

3. Tests of the method

3.1. Comparison with the Monte Carlo code

The new code was first tested against our Monte Carlo code (Juvela 1997) that has already been tested and has recently been compared with other radiative transfer codes (van Zaddelhoff et al. 2002). Tests of our new code were done using single-resolution grids and MHD cloud models similar to those used in Juvela et al. (2003). Models represent an interstellar cloud with a diameter of ~ 10 pc, average density 500 cm^{-3} and temperature of 10 K. Two supersonic models with Mach numbers $M = 2.5$ (model *A*) and $M = 10$ (model *B*) were used (for more details see Padoan et al. 2003). The resolution is 124^3 cells. Tests

were repeated for ^{13}CO and ^{12}CO so that average optical depths of the lowest transitions ranged from a few to over one hundred.

For the new ALI code we first used a discretization where all the cells were subdivided twice and the resulting cells exactly corresponded to the 124^3 cell grid of Monte Carlo calculations. Line intensities from the Monte Carlo code and the new code agree very well. The difference in average intensity is less than 1%, and rms differences computed over maps of 124×124 spectral lines are below $\sim 2\%$. The remaining variations can be explained with sampling errors caused by the finite number of simulated photon packages in Monte Carlo (800,000 per iteration) and the finite number of directions (~ 40) in the ALI runs. In both codes the cloud description is practically identical and the cloud consists of cells which are internally homogeneous. For example, in ALI calculations we do not interpolate source functions and absorption coefficients when the radiative transfer equation is integrated along a SC. The main difference between the two methods is the following. In the Monte Carlo code the local intensity is described through the number of absorbed photons, which is the result of integration along random lines of sight through a cell. In the new ALI code the intensity is calculated for the central position of each cell. The two results may differ if there is a large difference between the radiation field at the cell centre and at the cell boundaries. This is possible only if individual cells are optically very thick. The small difference in the results from the two codes shows that this effect is not important for the current models. The small differences between the maps produced by the two codes are also of a random nature, and do not correlate for example with the position of dense filaments.

Convergence was checked with and without ALI acceleration. All calculations were started with LTE level populations assuming excitation temperature equal to kinetic temperature. This is a better approximation for dense gas than for lower density regions where the converge is fast anyway. Fig. 4 shows the convergence in model A. For ^{13}CO the difference between the two methods is small but for optically thick ^{12}CO the ALI method is significantly faster. Another noticeable feature is the non-linearity (on a logarithmic scale) of the convergence. Initial fast convergence is due to the low-density gas where the relative change in the level population, $\Delta n_i/n_i$, becomes small very quickly. At later iterations, the average convergence rate depends on gradually more opaque regions where convergence is slower. The ALI method improves the convergence in opaque regions and the change in the overall convergence rate versus the number of iterations is much smaller than for the lambda iteration method. However, an inhomogeneous cloud always has regions with different convergence rates and the initial behaviour is generally not a good indicator of the convergence rates after many iterations.

3.2. Tests of multi-resolution calculations

We now report on the comparison between single-resolution (SR) and multi-resolution (MR) models with three levels hierarchy. In MR calculations part of the level 1 cells are divided into eight level 2 cells and each of these may in turn be divided into eight level 3 cells. On lower levels (i.e. for larger cells) density and velocity are averaged over sub-cells, and the intrinsic line-width is calculated taking into account velocity dispersion between sub-cells. Level 3 cells correspond exactly to cells in the SR models. The comparison between SR and MR models allows us to test the accuracy of the MR code as a function of the number of computational cells. MR models are useful only if a reasonable accuracy is achieved with a number of computational cells significantly smaller than in the SR models. The ratio between the number of cells in the MR and SR models, R , is roughly proportional to the ratios in computational times and in the memory requirements of the two models. It should be kept as low as possible, provided the spectral line profiles are computed with the required accuracy.

For the purpose of this comparison we have used a refinement criterion based on the local gas density. A large fraction of the cloud volume is filled with low-density gas. Unless optical depths are very high, only dense parts are relevant for a comparison with observational data, while the rest of the volume can be modelled at a low resolution. In the two MHD models we have used in this work the average density is 500 cm^{-3} , while peak values are higher by a factor of 33 for model *A* and a factor of 170 for model *B*. The rms error of the ^{13}CO line intensities was computed as a function of the threshold density for refinement. In model *B*, an accuracy of 10% is reached with $R \sim 0.1$, that is with computations that are one order of magnitude faster than for the SR model (see Fig. 5 and Fig. 6). In model *A* the density contrast is lower but accuracy turns out to be even slightly better.

The accuracy is expected to be better for species that are optically thinner or have higher critical densities than ^{13}CO since for these the emission will be even more concentrated in the densest regions. Conversely, for optically thick molecules, one might think that good accuracy would require higher R values. A larger fraction of cloud volume becomes relevant for observed lines but, on the other hand, excitation temperature variations are decreased by line thermalization. For ^{12}CO the average optical depth of the $J = 1 - 0$ line is in our model clouds ~ 100 . An accuracy of 10% is reached for both models with $R \lesssim 0.15$. This is not very different from the value of R required for the ^{13}CO line. However, an accuracy of 5% is achieved for the ^{12}CO line only with values of R above 0.5, making the advantage of the MR calculations very small if high precision is required for such optically thick lines. By modifying the molecular abundance we calculated a few models with average optical depths between the previous ^{13}CO and ^{12}CO models. These confirmed a gradual decrease of

accuracy with increasing optical depth. Higher discretization in optically very thin regions does little to improve the accuracy of computed spectra. The same seems to apply to very high optical depths. If one assumes a constant kinetic temperature also the excitation is in these regions nearly constant and because of the foreground absorption these regions contribute directly only little to the observed intensity.

Apart from the velocity field the main factors affecting the accuracy of the MR calculations are line optical depth and the inhomogeneity of the cloud model. Previous tests showed that calculations are feasible for a wide range of optical depths, at least in the range $\tau \sim 1$ -100. For higher depths one could improve the efficiency by using smaller cell size on that side of the cloud that is facing the observer - provided that it is sufficient to calculate the spectra just for one viewing direction.

The small difference between the two model clouds suggests that accuracy is not strongly dependent on the density distribution. However, both models are rather clumpy and one might ask whether the situation might change in more homogeneous clouds where observed intensities are again affected by a larger fraction of the cloud volume. We modified the density contrast of model *B* and checked the effect this has on the accuracy of ^{13}CO spectra. The average density, $n=500\text{ cm}^{-3}$, was kept constant while density variations were decreased by a factor of 2, 5, 10, or 50. Cells above a density limit of $n=500\text{ cm}^{-3}$ were split so that the discretization was in all cases exactly the same. In the original model the rms error of line intensities was slightly below 6% (see Fig. 5). The error increased with decreasing density variations but was still less than 12% when density contrast was decreased by a factor of 50. The result is not altogether surprising. Fine discretization is needed in order to resolve variations in density and excitation. In a homogeneous cloud these variations become small and errors resulting from a poor discretization do not grow very large.

It may be possible to define a better criterion for cell refinement if information on excitation temperature (T_{ex}) and velocity fields is included. The excitation temperature is the most important variable affecting the emerging intensity, although its variations mostly follow density variations. Good sampling of the velocity field would be particularly important if we were interested in line profiles rather than total line intensities. Velocity field determines the radiative coupling between different areas and the spatial resolution in regions of high velocity gradients could have an impact even on line intensities.

As an alternative refinement criterion we set threshold values for velocity difference, ΔV , and excitation temperature difference, ΔT , and refine all cells where such differences relative to neighbouring cells are above a given threshold. All combinations of ΔV and ΔT thresholds resulted in an accuracy that was always worse or only roughly equal than with the simple density criterion with equal values of R . The ΔV and ΔT limits force the refinement

in all regions with velocity and excitation gradients, even in low density regions which do not contribute much to the observed spectra. This may explain the relatively poor result. On the other hand, these tests show that density does indeed provide a good criterion for hierarchical refinement. With a suitable combination of density, excitation temperature and velocity criteria one does obtain better results. The improvement is, however, only $\sim 1\%$ in accuracy for any given value of R and in the following we rely only on a density thresholds.

Spectral line maps were computed toward three orthogonal directions using both full resolution and multi-resolution models. The maps were used to test the accuracy of spatial power spectra obtained with multi-resolution calculations. Least square fits to the power spectra were computed in the interval $k=0.3-5\text{ pc}^{-1}$. In the case of the full 124^3 SR model the Nyquist limit is 6.2 pc^{-1} and, for the grid of lowest resolution (level 1 of the MR model), one fourth of this value, 1.55 pc^{-1} . Fig. 7 shows results for ^{13}CO spectra from model B where the density threshold for refinement was 2000 cm^{-3} . In this case, $R=5\%$ (factor of 20 reduction in computational time and memory requirement) and the slope of power spectra is recovered with an accuracy of $\sim 1\%$. This can be compared with the difference between the slopes of line intensity and column density power spectra which is at least three times and on the average about ten times larger. Table 1 shows results for both models (A and B) and both molecules (^{13}CO and ^{12}CO) when cells above $n = 500\text{ cm}^{-3}$ are refined.

4. Comparison with LTE- and non-isothermal models

We have used the new ALI multi-resolution radiative transfer code to study differences in statistical properties between LTE and non-LTE spectra and between isothermal and non-isothermal models. Non-LTE non-isothermal models provide the closest descriptions to real interstellar clouds. However, LTE and isothermality are often assumed when MHD simulations are compared with observations. It is therefore important to quantify the uncertainties caused by these assumptions.

The cloud model used for this purpose is based on an MHD simulation performed on a uniform cartesian grid of 350^3 computational cells. In order to make the grid divisible by four we took from this 340^3 cells. The simulation represents a cloud with a sonic Mach number $M \approx 10$ and an average density of $n = 500\text{ cm}^{-3}$ (for details see Padoan et al. 2004). We define a three level hierarchical refinement, where the root grid (level 1) consists of 85^3 cells. The grid is refined above a density threshold of $n > 500\text{ cm}^{-3}$. After two subdivisions the smallest cells are the same as in the full resolution model of 340^3 cells. The computational time is about one quarter of that needed at the full 340^3 resolution ($R \approx 0.26$). Based on previous tests, the rms error of line intensities should be below 6%. However, even

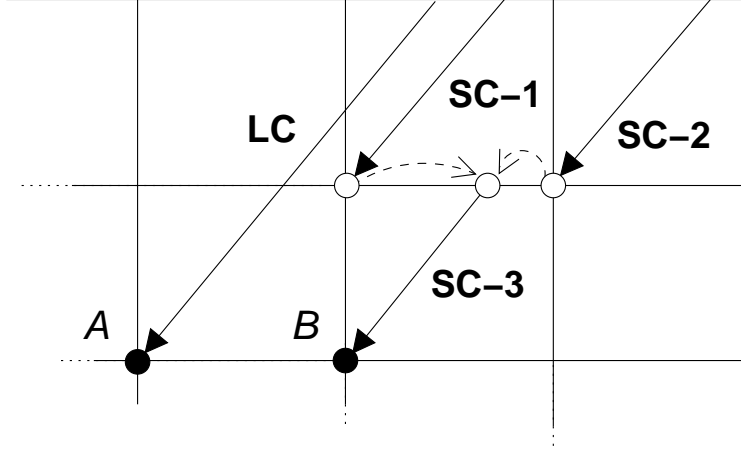


Fig. 1.— Two schemes for computing intensity at a grid position. With a long characteristic (LC) calculation is done by integrating directly from the cloud surface to a grid position A . Alternatively, the intensity can be propagated one grid layer at a time using short characteristics (SC). In the latter case interpolation (dashed arrows) is used to determine the intensity at the starting position of the third SC that ends at the grid position B .

Table 1: Accuracy of power spectra from the multi-resolution models where cells above $n=500 \text{ cm}^{-3}$ are refined. Columns are (1) model cloud, (2) R parameter, (3) slope of spatial power spectrum of column density, (4) molecule, (5) slope of spatial power spectrum of ^{13}CO intensity from the multi-resolution models. The slopes are averages of results obtained for three orthogonal directions. The average difference between slopes computed from the multi-resolution models and the full 124^3 cell models are given in parentheses in the last column

Cloud	R	$a(N)$	Molecule	$a(^{13}\text{CO})$
A	0.31	2.831	^{13}CO	2.641 (-0.027)
			^{12}CO	2.527 (+0.009)
B	0.24	2.475	^{13}CO	2.583 (+0.017)
			^{12}CO	2.570 (-0.015)

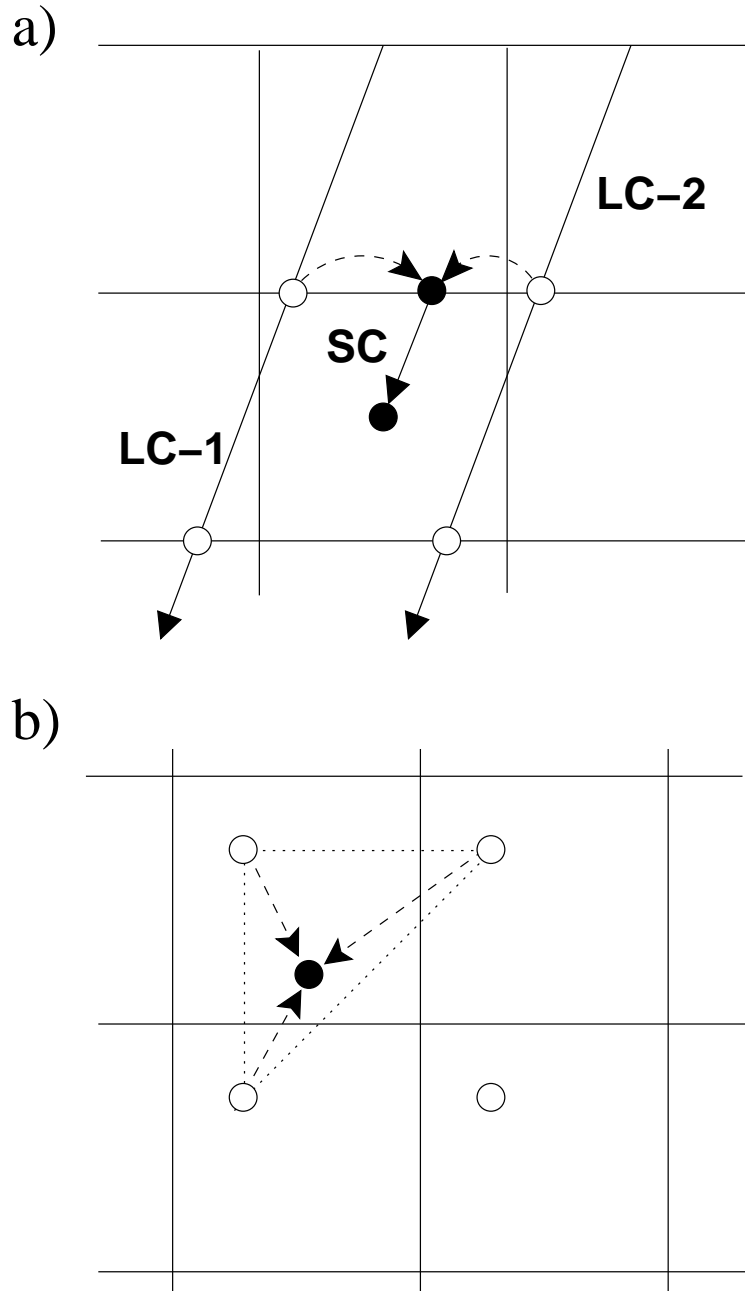


Fig. 2.— Our scheme for the propagation of intensity information. The grid denotes *cells* at the centre of which intensity is computed. Long characteristics (LC) are used to integrate the intensity, one cell layer at a time, so that accurate intensities are known at the cell faces (open circles). Interpolation (dashed arrows) is used to derive the intensity at the starting point of a short characteristic (SC) used to integrate the intensity to the centre of a cell (filled circle). The lower frame shows the situation from above: interpolation is done using the closest three LCs.

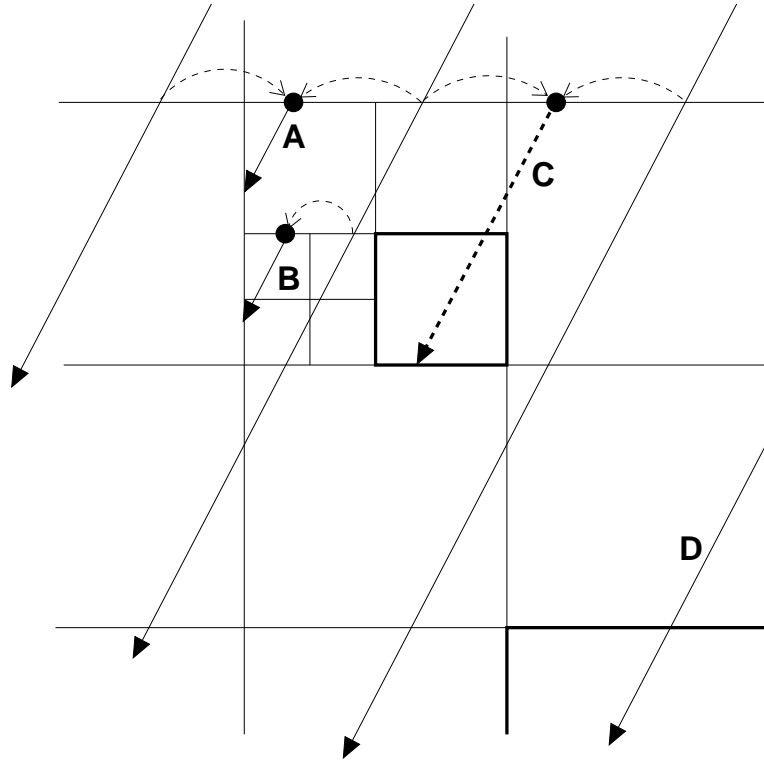


Fig. 3.—

Examples (in 2D) of the creation and deletion of LCs as the cell discretization changes along their path. Solid arrows stand for LCs and dashed arrows denote interpolation. The four long arrows are level 1 LCs that start at the cloud surface and are never deleted. *A* is a new level 2 LC that is created by interpolation of level 1 LCs and is deleted when it enters a level 1 cell. The intensity at the starting point of the level 3 LC *B* is taken directly from the nearest LC because level 2 LCs are not present on both sides. The LC *C* is created only later, at the time of the creation of SCs, when it is noticed that the top of the cell (thick box) is not hit by any of the existing LCs. The LC *C* is traced back to the previous cell boundary where interpolation takes place. Finally, the LC *D* is also created later and it is traced back to the cloud surface.

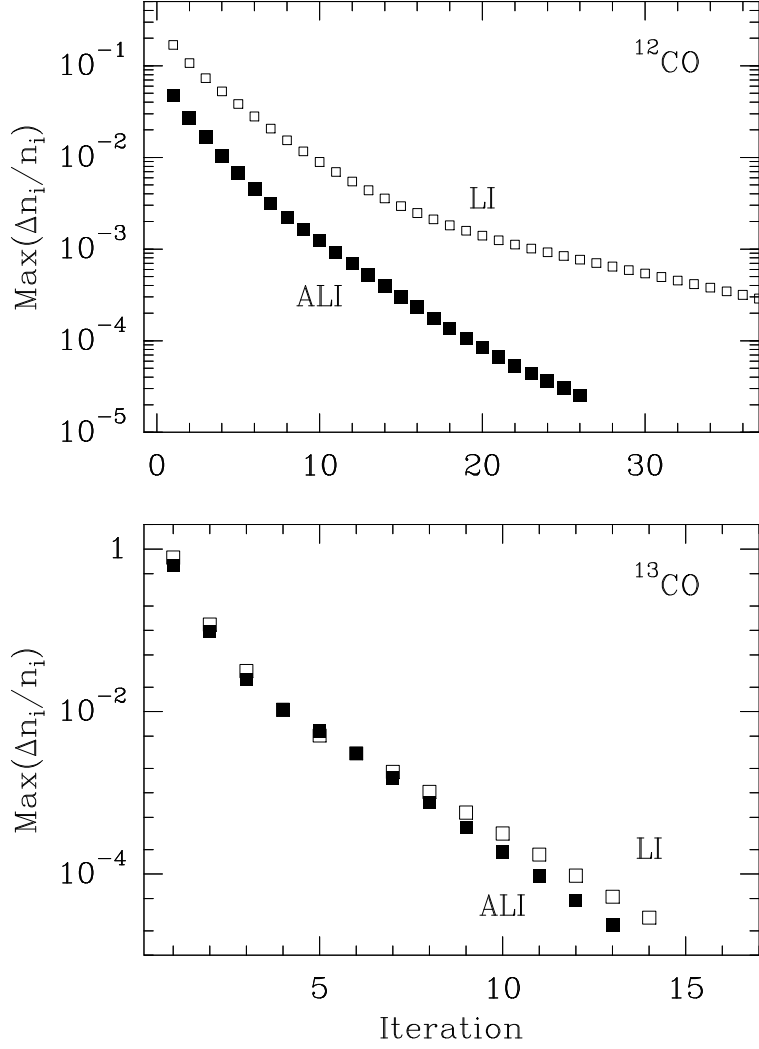


Fig. 4.— Convergence of ^{12}CO level populations with lambda iteration and accelerated lambda iteration in the case of the MHD model *A* with sonic Mach number 2.5. The maximum relative change in level population, $\Delta n_i/n_i$, was calculated for transitions up to $J = 4$ for each cell with $n > 50 \text{ cm}^{-3}$. The average of these values is plotted here. The average optical depth for the transition $J=1-0$ is ~ 4 and ~ 124 for ^{13}CO and ^{12}CO respectively.

better accuracy is expected because the total optical depths are similar as in Sect.3, but the resolution is higher.

4.1. Comparison with LTE calculations

Line observations are often studied with an 'LTE' analysis, which includes both assumptions of local thermodynamic equilibrium and constant excitation along the line of sight. Conversely, under the same assumptions spectral lines are easily predicted for any cloud model. The source function and the optical depth follow from the LTE conditions and the radiative transfer equation can be directly integrated along the line-of-sight. The LTE method is very often used in the analysis of observations and also to compare observations with MHD simulations. Although this method takes into account of some optical depth effects, it is extremely simplified considering the wide range of physical conditions present in any cloud.

We computed a non-LTE isothermal model with $T_{\text{kin}}=10$ K and compared it with spectra obtained under LTE conditions and assuming constant excitation temperature for the whole cloud. In a real cloud the excitation temperature varies from position to position and can take any value between the kinetic temperature and the temperature of the background radiation (2.7 K). We considered two LTE models, one with $T_{\text{ex}} = 10$ K and another with $T_{\text{ex}} = 5.5$ K. In the following we refer to the velocity integrated line intensity (measured in K km s^{-1}) simply as line intensity or line area. We find the average line intensity of the $T_{\text{ex}}=10$ K model is approximately 30% higher than in the non-LTE model, while it is approximately 15% lower in the $T_{\text{ex}} = 5.5$ K model. After subtracting the mean intensity, the remaining rms intensity scatter between the LTE model with $T_{\text{ex}} = 5.5$ K and the isothermal model is approximately 25%. This shows that there are significant differences in the spatial distribution of line intensities. Intensities of the $T_{\text{ex}} = 10$ K model are compared with the LTE model in Fig. 8.

We computed spatial power spectra based on the $^{13}\text{CO}(1-0)$ line areas. Least squares fits to these spectra are computed in the range of wavenumbers $k = 0.3 - 10.0 \text{ pc}^{-1}$. The upper limit is well below the Nyquist limit (the actual resolution of MHD simulation is slightly worse than the sampling). The slopes of the fits are given in Table 2. Differences are very small, of the order of a few per cent, compared with the large line area variations seen in Fig. 8. Apparently for lower T_{ex} the main effect is a decrease of power at all scales and the slope of the power spectrum is only slightly affected.

Replacing non-LTE level populations with LTE values decreases the excitation in dense

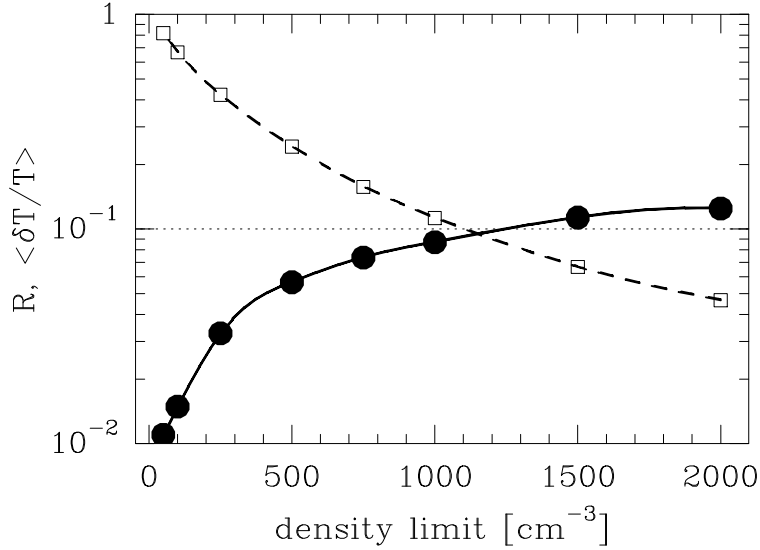


Fig. 5.— Accuracy of multiresolution calculations as a function of the density threshold for grid refinement. The rms-error in the computed intensities of the $^{13}\text{CO}(1-0)$ line (filled circles) and the value of the ratio of the number of cells in the MR and SR models, R , (open squares) are plotted versus the density threshold for model B . The plot shows results for model B but very similar values are obtained for model A .

Table 2: Slopes of spatial power spectra of ^{13}CO line area in the 340^3 cell non-LTE isothermal model with $T_{\text{kin}}=10$ K and in two LTE models with $T_{\text{ex}}=10$ K and 5.5 K. The last column gives the slopes for column density maps of the MHD model. Results are given for line area maps computed for three orthogonal directions (X , Y , and Z).

direction	$T_{\text{kin}}=10$ K	$T_{\text{ex}} = 10$ K	$T_{\text{ex}} = 5.5$ K	N
X	-2.621	-2.661	-2.628	-2.663
Y	-2.665	-2.691	-2.658	-2.688
Z	-2.674	-2.714	-2.642	-2.746

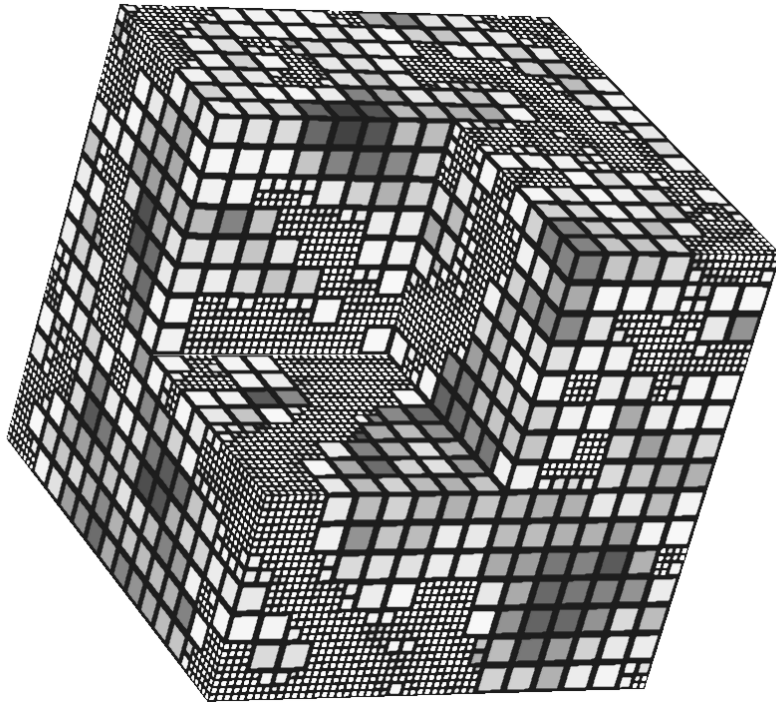


Fig. 6.— Discretization for model *A* with grid refinement above a density of 500 cm^{-3} . For clarity, this figure shows a model with a decreased resolution of 60^3 cells. One corner of the cloud has been extracted to show the discretization inside the cloud.

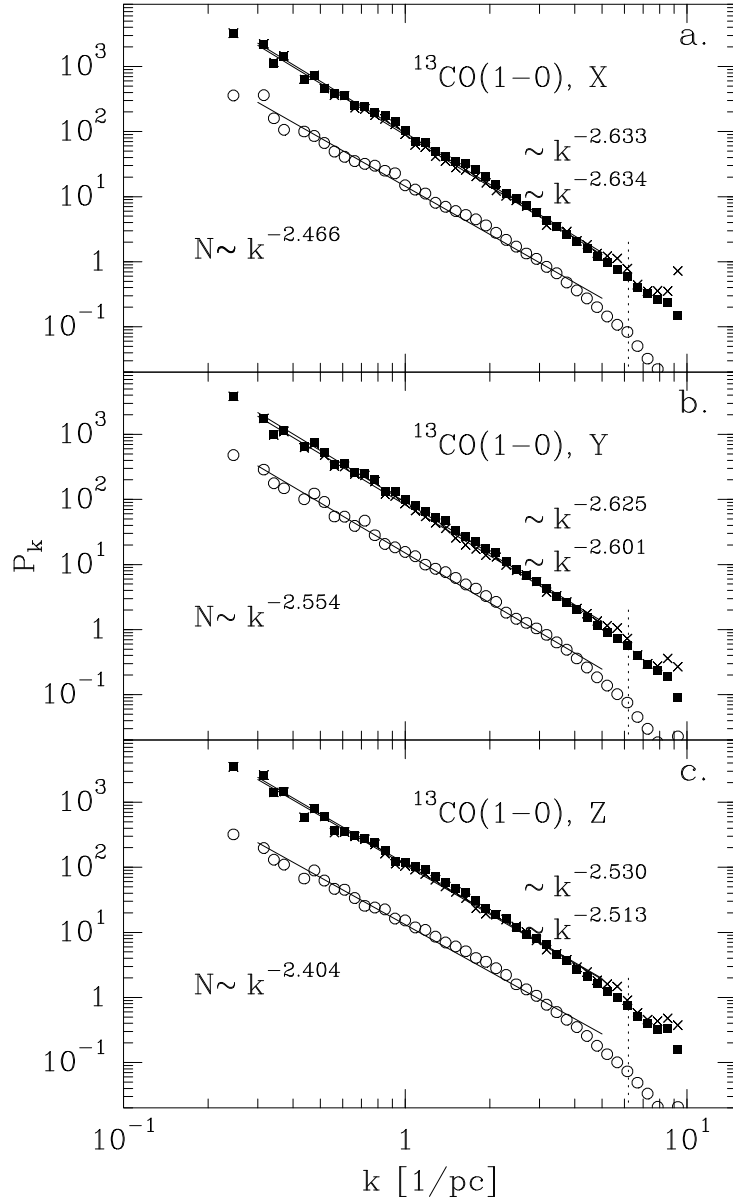


Fig. 7.— Spatial power spectra of the ^{13}CO line intensity and of the column density in model *B*. Frames correspond to maps computed for three orthogonal directions. Solid squares show the spatial power spectrum of the ^{13}CO emission from the full 124^3 cell model. Crosses show the same power spectra computed from multi-resolution models where cells with densities above 2000 cm^{-3} are refined ($R=0.047$). Open circles show the column density power spectra (the normalization is arbitrary). Solid lines indicate least squares fits in range $0.3\text{--}5 \text{ pc}^{-1}$. The slopes are indicated in the figure. Slopes for ^{13}CO are shown on the right hand side (the values for the multi-resolution models are below those for the full resolution models). The dotted vertical lines indicate the Nyquist limit for the full resolution model with 124^3 cells.

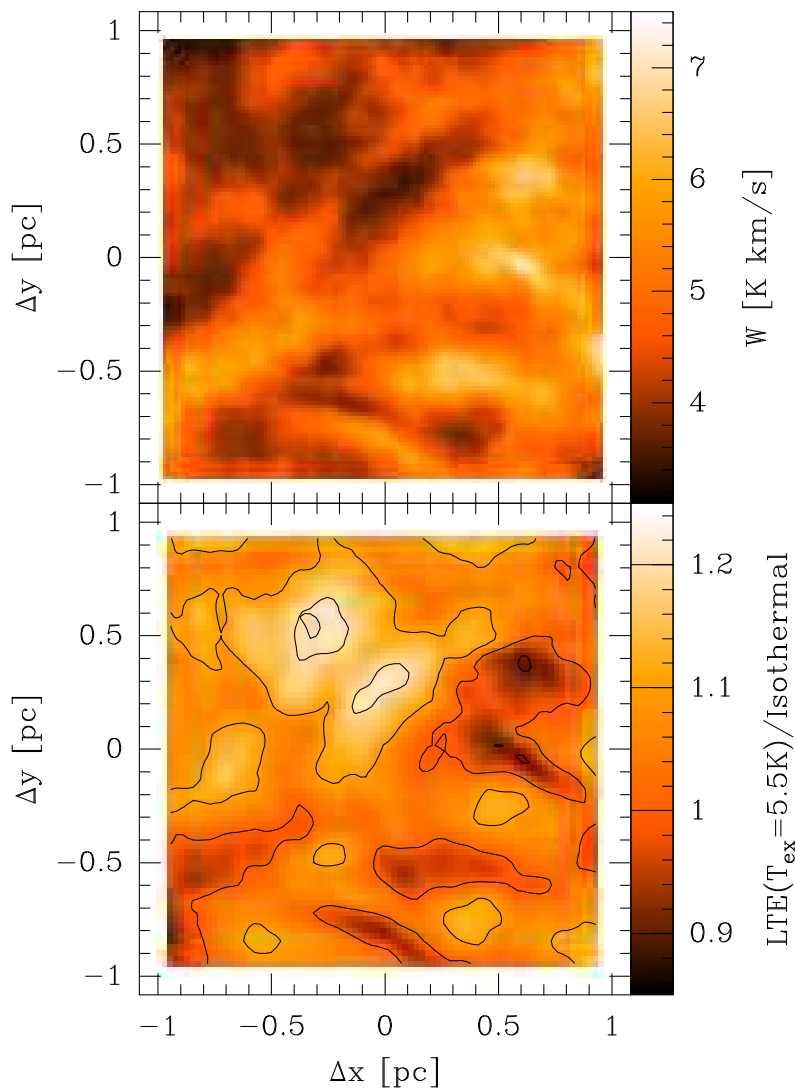


Fig. 8.— The upper frame shows a map of line intensities calculated from our non-LTE isothermal cloud model ($T_{\text{kin}}=10$ K). The lower frame shows ratio of line intensities between LTE-model with $T_{\text{ex}}=5.5$ K and the isothermal model. These images are restricted to a small region of 2×2 pc, while the full size of the model is 10×10 pc.

regions and increases it in the low density gas. This should make the spatial power spectra of the intensity maps closer to those of the column density. This is in fact the case of the $T_{\text{ex}}=10$ K model, where the slopes of the power spectra of line areas are almost identical to the slopes of the column density maps, within the numerical accuracy. The accuracy of the computed slopes should be better than ~ 0.01 (see Table 1) because the same multi-resolution cell discretization is used for the three models. For excitation temperature $T_{\text{ex}}=5.5$ K the slopes are closer to those of the isothermal model and, apart from the X -direction, slightly lower. The overall differences between the three clouds are small and mostly reflect average excitation temperatures. For such cold clouds small temperature differences correspond to large changes in optical depth. At $T_{\text{ex}}=5.5$ K the optical depth of the $J = 1 - 0$ line is already more than twice the value at $T_{\text{ex}}=10$ K. Larger differences between line maps and column density maps are therefore expected for the $T_{\text{ex}}=5.5$ K model than for the $T_{\text{ex}}=10$ K one.

This comparison of LTE and non-LTE spectra is different from the issue of the accuracy of LTE column density estimates (see e.g. Padoan et al. 2000). Padoan et al. (2004) analysed simulated ^{13}CO spectra and concluded that the power spectrum of column densities derived from observations under the LTE assumption was generally steeper than the power spectrum of the underlying column densities. One reason is that as ^{13}CO lines become saturated in the densest parts of the cloud the column densities are underestimated there and also the power at small scales is reduced. The effects of such self-absorption are directly visible in line profiles only for optically thicker species.

Another reason may be linked with excitation temperature gradients. In LTE calculations T_{ex} is usually based on the brightest regions where T_{ex} is above the average value. This means that in regions of lower density (and lower T_{ex}) column densities are underestimated. If this introduces additional gradients between centre and edges of the column density map this will add power at large scales and make the power spectrum steeper. On the other hand, the same effect can work also at small scales. In particular, if the excitation temperature in a core is higher than assumed the computed column density will also be too high and additional power is introduced at the smallest scales.

4.2. Comparison with non-LTE non-isothermal models

Padoan et al. (2004) computed kinetic temperatures for similar model clouds by balancing cosmic ray heating with cooling by line emission from the most important species. This resulted in a relation between the gas kinetic temperature (see Fig. 9). We use this relation to compute non-LTE non-isothermal spectra for our 340^3 cell model. These spectra should provide a better description of observational data than the isothermal ones.

Because the kinetic temperature decreases as a function of density one would expect emission from dense cores to be decreased, as in the LTE models. This is to some extent visible in Fig. 10, where cores with the brightest ^{13}CO emission are weaker in the non-isothermal case than in the isothermal one. However, differences from the LTE model (Fig. 8) are also significant, due to the large range of kinetic temperatures in the non-isothermal cloud.

Fig. 11 shows average $^{13}\text{CO}(1-0)$ and $^{13}\text{CO}(2-1)$ spectra. The profiles of the averaged spectra are smooth but significant differences are seen in the line ratios between the LTE and the non-LTE models. Differences are also visible in $^{13}\text{CO}(1-0)$ profile ratios plotted in the lower panel of Fig. 11. Compared with the isothermal cloud the LTE model with $T_{\text{ex}}=10$ K has weaker line wings while for the LTE model with $T_{\text{ex}}=5.5$ K the opposite is true. The optical depth of the cold LTE model is much higher than in the warmer LTE model, so the profile reflects more the velocity structure on the observer side of the cloud. The non-isothermal model shows stronger line wings that result from the fact that in this model kinetic temperatures are higher in the more rapidly moving low density gas. This should also be the case for observed spectra of molecular clouds, as similar kinetic temperature variations should also be present in real clouds.

Differences between models are even stronger in the profiles of individual spectra, as shown in Fig. 12. In some velocity intervals, spectra may be almost identical, while at other velocities differences between the LTE and the non-LTE non-isothermal models can exceed a factor of four. Despite the differences in the peak temperature of non-isothermal and isothermal models (over a factor of two) the shape of the spectral line profiles are similar in these two models. Spectra from the LTE model show both different peak temperatures and spectral shapes relative to the non-LTE models.

Fig. 13 shows ratio of line areas, $W[^{13}\text{CO}(2-1)]/W[^{13}\text{CO}(1-0)]$, for non-LTE-non-isothermal and LTE models divided by the same line area ratios in the isothermal model. In both cases, variations up to 40% are found.

Differences in the spatial power spectra calculated based on the $^{13}\text{CO}(1-0)$ line areas are very small, with the slopes of the non-isothermal model steeper by only $\sim 1\%$. The shape of the T_{kin} vs n relation is such that the model cloud is almost isothermal at the highest densities. Some of the differences between the isothermal and non-isothermal models may well be caused by a difference in the average kinetic temperature, which affects the optical depths. In the case of the LTE models we found a flattening of the spatial power spectra with decreasing excitation temperature (increasing optical depth). The spatial power spectra are flatter for the non-isothermal model which is consistent with the average kinetic temperature being below 10 K.

The correlation between kinetic temperature and local gas density plotted in Fig. 9 contains a significant amount of scatter. There is some noise arising from the used Monte Carlo calculations. However, most of the scatter is real, showing the kinetic temperature does not depend only on the local gas density but also on the shielding provided by neighbouring regions. In particular, the kinetic temperature distributions as calculated in Padoan et al. (2004) have large scale structure with temperature decreasing toward centre of the cloud. When we use the fit shown in Fig. 9 we ignore this variation and consequently we subtract power from the large scales.

Such large scale gradients affect also the reverse process of estimating column densities from observations using the LTE analysis. When a constant excitation temperature is determined from the dense central regions the excitation is progressively over-estimated as one moves toward the cloud edges. At the same time the ratio between estimated column density and the true column density falls below one. In other words, column density gradients between centre and cloud edge are artificially increased, more power is introduced at large scales and one obtains a spatial power spectrum that is too steep (i.e. steeper than the corresponding spectrum of true column densities). This may be the reason why Padoan et al. (2004) found a large difference between the slopes of LTE column density estimates and true column density. They estimated this difference to be 0.13 ± 0.06 . In our case differences between different cases are about 0.04 or below but by construction our models do not have similar T_{kin} gradients. We should again point out that our comparison between LTE and non-LTE models is different from the problem of estimating LTE column densities from observations. However, if our interpretation is correct, the effects that such large scale temperature gradients (in T_{ex} amplified by T_{kin} gradients) have on spatial power spectra slopes can be as significant as differences between e.g. LTE and non-LTE calculations.

5. Discussion

Comparison of LTE and non-LTE models showed significant differences in line profiles but differences in spatial power spectra were relatively small. The slopes of the power spectra depend, however, on the assumed excitation temperature since that determines the line optical depths. For example, in Table 2 at high temperatures (low optical depths) the LTE slope approaches that of the column density distribution and at low temperatures (high optical depths) the spectrum becomes more shallow than in non-LTE calculations. If one is interested *only* in the slope of the power spectrum and an accuracy of a few per cent is sufficient then LTE calculations can be used to predict line intensities. When results are compared with observations it is also better to use LTE predictions rather than column

densities read directly from the cloud model. In our models the differences between power spectra of column density and non-LTE line intensities were less than 3%. Therefore, if one considers only power spectrum slopes then non-LTE calculations are necessary only in quite detailed studies. However, they are still required if absolute line intensities, line ratios or line profiles are being studied.

The spatial power spectra were fitted with power laws $P \sim k^{-a}$. The slopes a were found to depend on two factors, the average optical depth and the general cloud structure. In most cases (models *A* and the large 340^3 cell models) the power spectrum is flatter for line emission than for the underlying column density distribution. Furthermore, a decreases with increasing optical depth, as seen by comparing the results for ^{13}CO and ^{12}CO . However, if the slope of the column density spectrum is shallow (a below 2.5) the spectrum of line emission can become the steeper of the two and the effect of optical depth on a is reduced or may even be reversed. For model *B* all ^{13}CO maps and two of the three ^{12}CO maps have power spectra that are steeper than the spectra of the corresponding column density maps. For the direction z the slope a is also steeper for the ^{12}CO map than for the ^{13}CO map. The trend is clear: as the slope of the column density becomes more shallow the difference between ^{12}CO and ^{13}CO maps decreases (see Table 3) and only in the case of the smallest slope ($a \sim 2.4$) the spatial power spectrum of the optically thicker species is the steeper one.

In the optically thin limit the slopes of line emission and column density power spectra are identical. As the optical depth increases the densest cores are the first ones to become optically thick and emission from those regions saturates. Assuming the cores are very compact (as in model *B*) power is removed from the smallest scales and the spatial power spectrum of line emission becomes steeper. Clearly this explanation does not apply e.g. to model *A* since there the spectrum becomes more shallow instead. The actual optical depth dependence can be quite complicated and this can be seen even from LTE models not including effects that result from spatial variations of the excitation temperature. Fig. 14 shows the change in the slope of the spatial power spectrum as a function of the average optical depth in models *A* and *B*. For these LTE models a constant excitation temperature of 10 K was assumed and the molecular abundance was scaled to produce clouds with different optical depths.

In non-LTE calculations for model *A* the spatial power spectrum of line emission is less steep than the spectrum of the corresponding column density map. The opposite is true for model *B*. This is also illustrated in Fig. 14, which shows results from LTE models with a wider range of optical depths. Differences between column density and line maps increase at least up to $\langle \tau \rangle \sim 100$ when most of the sightlines are already optically thick. However, the change is non-linear and depends on the actual density distribution and on the order in

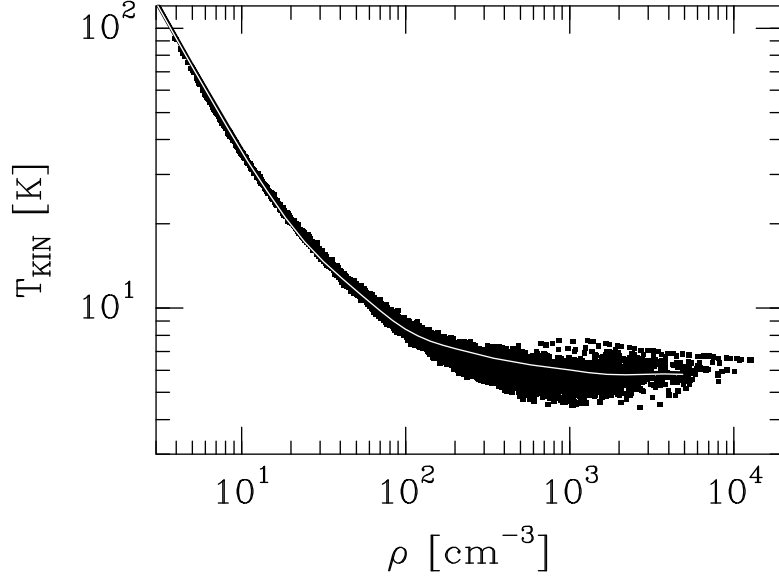


Fig. 9.— Kinetic temperature as the function of local density (for details see Padoan et al. 2004). The solid line represents a fit that was used to set the kinetic temperature in our non-isothermal model.

Table 3: Comparison of spatial power spectra computed for ^{12}CO and ^{13}CO maps. The non-LTE spectra were computed for isothermal models with $T_{\text{kin}}=10$ K. The columns are: the model cloud, the viewing direction, slope of the column density power spectrum (a_N), slope of the spatial power spectrum for ^{13}CO emission and the difference in the slopes between ^{12}CO and ^{13}CO power spectra. Maps are listed in increasing order of the slope a_N .

model	direction	a_N	$a(^{13}\text{CO})$	$a(^{12}\text{CO}) - a(^{13}\text{CO})$
<i>B</i>	<i>z</i>	2.40	2.51	+0.11
<i>B</i>	<i>x</i>	2.47	2.63	-0.06
<i>B</i>	<i>y</i>	2.55	2.60	-0.08
<i>A</i>	<i>z</i>	2.71	2.61	-0.05
<i>A</i>	<i>x</i>	2.85	2.65	-0.12
<i>A</i>	<i>y</i>	2.93	2.66	-0.16

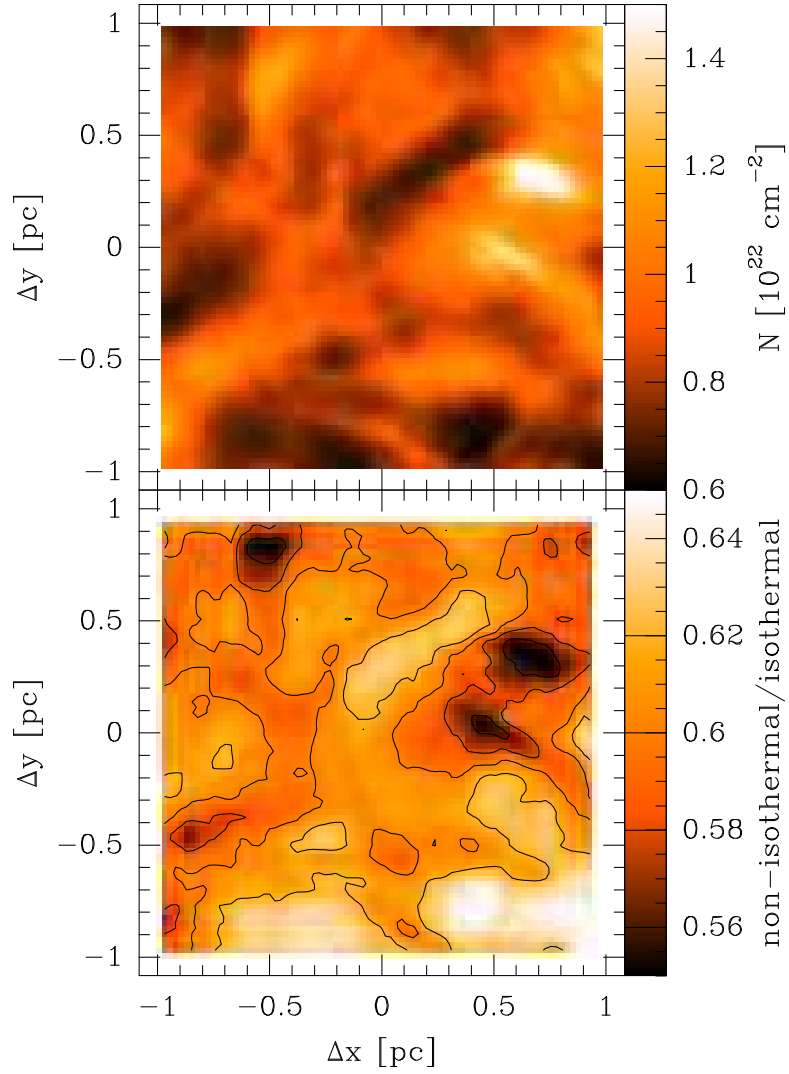


Fig. 10.— The upper frame shows the column density around the centre of the model cloud. The lower frame shows the ratio between $^{13}\text{CO}(1-0)$ line areas in non-isothermal and isothermal models. The images are limited to a region of 2×2 pc. The full size of the model is 10×10 pc.

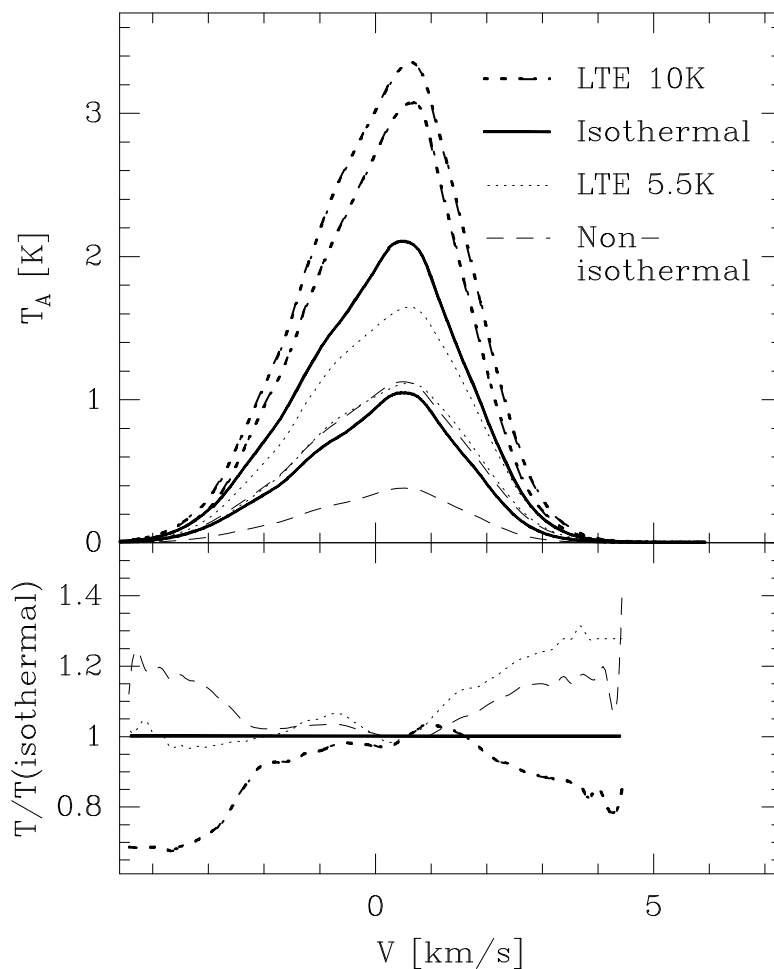


Fig. 11.— The upper panel shows the average $^{13}\text{CO}(1-0)$ and $^{13}\text{CO}(2-1)$ spectra from the isothermal model, the non-isothermal model and the LTE model of Sect. 4.1. The $J = 2 - 1$ line is stronger than $J = 1 - 0$ line only in the case of LTE model with $T_{\text{kin}}=10$ K. The spectra are averaged over the whole spectral line map computed for the X direction. The lower panel shows $^{13}\text{CO}(1-0)$ line profiles normalized to the same peak value and divided by the average profile of the isothermal model.

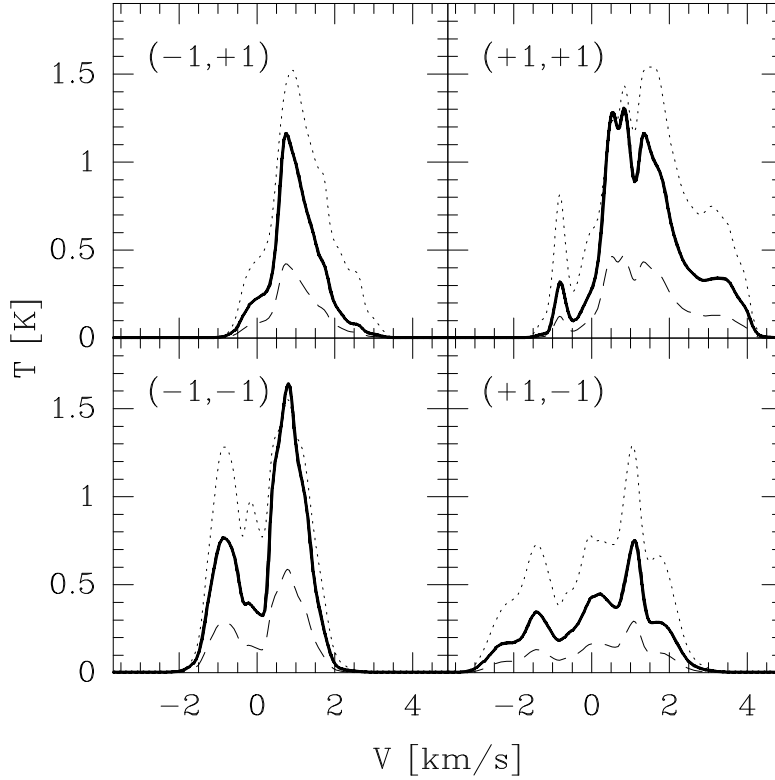


Fig. 12.— A few $^{13}\text{CO}(2-1)$ line profiles computed for non-LTE isothermal and non-isothermal models and for the LTE model with $T_{\text{ex}}=5.5\text{K}$. Spectra are calculated toward the X direction and averaged over an area of 0.04pc^2 . Positions are given in the figure as offsets in parsecs from the map centre. These positions correspond to the corners of the map shown in Fig. 10.

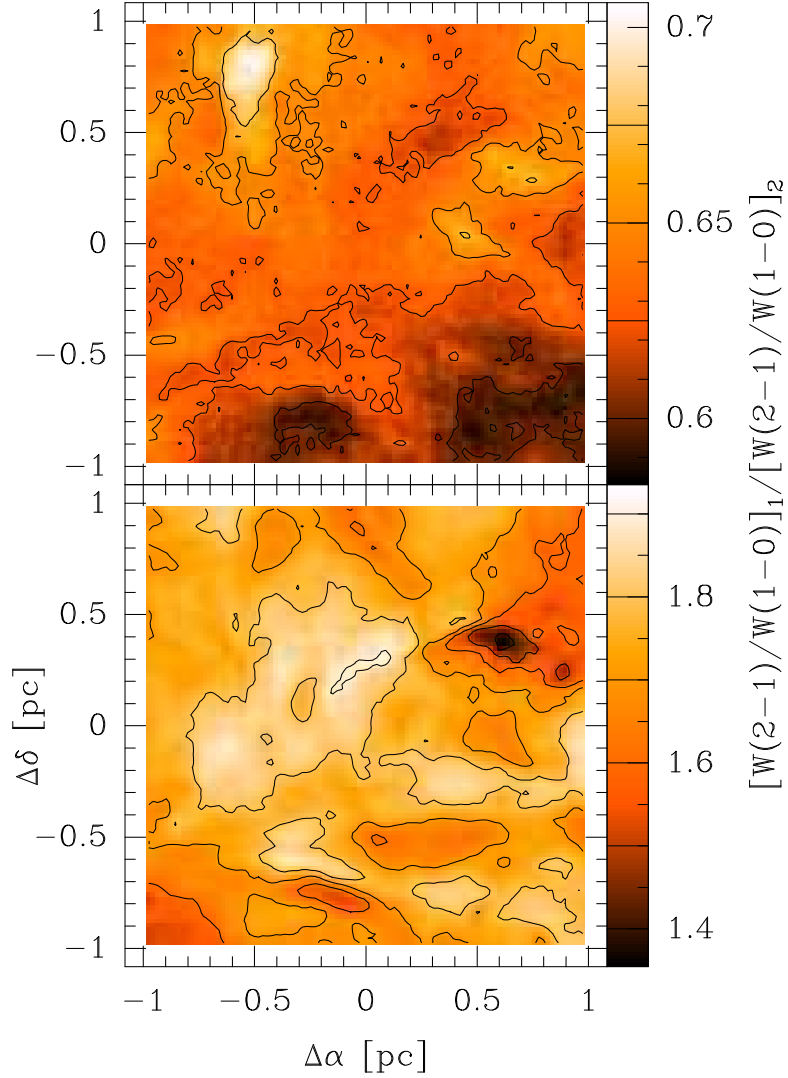


Fig. 13.— Line ratios $^{13}\text{CO}(2-1)/^{13}\text{CO}(1-0)$ in relation to the isothermal model. The upper frame shows the ratio of integrated line areas in the non-isothermal model divided by the ratio in the isothermal model. The lower frame shows line ratios from the LTE model with $T_{\text{ex}}=5$ K divided by line ratios from the isothermal model. Only the central region of 2×2 pc is shown.

which different regions become optically thick. Furthermore, the a vs. τ curves can be very different even when the same model cloud is viewed from different directions.

The slopes from non-LTE calculations with model B are marked in Fig. 14. For ^{13}CO map ($\langle \tau \rangle = 2.1$) the slope is steeper than when LTE conditions were assumed. In our non-LTE model the excitation temperature is lower than in the LTE-model and optical depth of the $J = 1 - 0$ transition tends to be higher. As a result, in the figure the mass of the non-LTE cloud is smaller than the mass of a LTE cloud with the same average optical depth. The non-LTE point corresponding to ^{12}CO map ($\langle \tau \rangle = 133$) is again below the curve of LTE models. At least in this range, the optical depth dependence of non-LTE models is different from that of LTE models.

The tests of Sect. 3 showed that multi-resolution models can provide significant savings in computational time and memory. An accuracy of approximately 10% was obtained in ^{13}CO calculations with $R \sim 0.1$. This corresponds to a factor of ten reduction in computational time and memory requirements (see also Appendix A).

In this paper we have computed spectral line maps over entire model clouds. Multi-resolution models provide, however, a general framework with which we can easily direct our attention to selected parts of a larger model cloud. For example, if we are interested only in one core we can use a discretization that becomes more coarse as distance between our line-of-sight and the core increases. In other words, long distance interactions between the core and the rest of the cloud are all included but are treated in a more approximate way. This can lead to very low R values ($\sim 1\%$ or below) making such radiative transfer calculations feasible for parts of future large MHD simulations (such as simulations of core collapse in large turbulent clouds computed with AMR methods).

6. Conclusions

We have presented a radiative transfer code for line transfer calculations on hierarchical grids. In interstellar clouds, dense gas responsible for the observed molecular lines has a small volume filling factor. As a result, fine discretization is needed only in a limited sub volume and hierarchical grids can significantly reduce both time and memory needed for radiative transfer simulations. The code was tested using cloud models that were based on MHD simulations. In particular we looked at the parameter R which is the ratio between number of cells in the hierarchical grid and in the corresponding single resolution grid (equal size of the smallest cells). According to these tests:

- for lines with optical depths $\tau \sim 1$ a 10% accuracy of computed line intensities is reached

with $R \sim 0.1$

- for optically thick lines ($\tau \gtrsim 100$) an accuracy of 10% is reached with $R \sim 0.15$
- if higher accuracy is needed the required number of cells increases rapidly: in the case of high optical depths a 5% accuracy of line intensities requires already $R > 0.5$ and the advantage of hierarchical grids becomes small
- the spatial power spectra recovered from hierarchical models were found to be accurate: with $R = 0.05$ errors in the slopes of the power spectra were only $\sim 1\%$

Using the new radiative transfer program we computed ^{13}CO spectra for one model cloud (340^3 cells) first for LTE conditions and then with full radiative transfer calculations assuming either isothermal or non-isothermal conditions. The comparison of the results showed that

- the LTE models differ clearly from the non-LTE models - not only in line intensities but especially in the shape of the line profiles
- the differences in the slopes of spatial power spectra, a , are small ($\lesssim 2\%$) and the main effect is a slight steepening of the power spectra with increasing excitation temperatures
- there is some indication that large scale gradients in kinetic temperature between cloud centre and surface (not included in our models here) may produce a steepening of the power spectrum that is larger than the differences between the models considered in this paper
- the difference between spatial power spectra of column density and line intensities was found to depend on both optical depth and cloud structure
- in models with relatively little small scale structure ($a \gtrsim 2.5$) the slope of the spatial power spectrum is more shallow for line emission than for column density and becomes even flatter with increasing optical depth
- in a more ‘clumpy’ cloud ($a \lesssim 2.4$) the situation may be reversed: line emission has a steeper power spectrum and slope increases with optical depth

M.J. acknowledges the support of the Academy of Finland Grants no. 175068, 174854, 1201269, and 1206049.

A. Implementation of multiresolution calculations

The implementation presented in this paper is optimised for low memory requirement. This is in part achieved by simulating each transition separately, and by writing intensities at cell centres to external files before proceeding to simulation of the next transition. The separate handling of transitions introduces an overhead that can be removed at the cost of an increased memory consumption. In our scheme, the intensities of the incoming radiation are kept in memory for one layer of level 1 cells and their sub-cells. These intensity values correspond to a significant fraction of total memory requirements. If all transitions were simulated simultaneously, memory requirement would increase by a factor almost equal to the number of transitions. On the other hand, because intensities are needed only for one layer of cells, the size of these arrays increase only proportionally to L^2 where L is the number of cell layers in the full-resolution model (i.e. full resolution model would contain L^3 cells). The use of external files for centre intensities (one value per transition per cell) may be more significant for the run times. These values can be kept in main memory only for small models since their number increases proportionally to L^3 .

For illustration we can look at the memory requirements of the computations presented in Sect. 4 where L was 340. One cell layer consists of $(L/4)^2$ level 1 cells, each containing down to level 2 a maximum of 64 sub-cells. If each transition is treated separately and intensities are simulated using ~ 100 frequency points the maximum storage requirement equals $\sim (340/4)^2 \times 64 \times 100$ floating point numbers i.e. some 180MB. The space needed to store average intensities in cells is $R \times L^3 \sim 0.25 \times 340^3$ numbers which equals about 40MB per transition. Additional space is needed for storing basic cloud data (cell velocities, densities, doppler widths etc.) and data needed for simulation of one transition (optical depths, source functions). These amount to ~ 300 MB but are mainly kept in external files.

For a cloud consisting of a regular grid of level 1 cells there is no overhead from the machinery that exists for handling multiresolution grids. For hierarchical grids the computations do, however, become somewhat more complicated. We take as an example model B where cells above density limit $n = 500 \text{ cm}^{-3}$ were divided and the value of R was 0.24. Compared with full grid (124^3 level 1 cells) the run time dropped to 0.27 times the original. This is quite close to that actual value of R and shows that it is a good indicator of the reduction in run times.

We have computed multi-resolution models with a maximum of three levels in the cell hierarchy. Deeper hierarchies are needed in the case of large MHD simulations on uniform cartesian grids with $L \sim 1000$ or for MHD simulations with AMR methods, where grids with many levels of refinement can be generated. In our current scheme each individual cell can be sub-divided independently. This is optimal as far as the R values is concerned but

may become inefficient for deeper hierarchies. Therefore, an alternative gridding scheme is being developed which will use continuous rectangular regions with fixed cell sizes. There the hierarchy will consist not of subdivided cells but of sub-volumes with smaller cell sizes.

REFERENCES

- Abel T., Bryan G.L., Norman M.L. 2004, *Science*, Vol. 295, Issue 5552, 93-98
- Auer L., Bendicho P.F., Bueno J.T. 1994, *A&A* 292, 599
- Auer L.H., Paletou F. 1994, *A&A* 285, 675
- Bernes C. 1979, *A&A* 73, 67
- Choi M., Evans II N.J., Gregersen E.M., Wang Y. 1995, *ApJ* 448, 742
- de Avillez M.A., Berry D.L. 2001, *MNRAS* 328, 708
- Dullemond C.P., Turolla R. 2000, *A&A* 360, 1187
- Falgarone E., Phillips T.G. 1991, *Signatures of Turbulence in the Dense Interstellar Medium*, Falgarone E., Boulanger F., Duvert G. (eds), *Proc. IAU Symp. 147, Fragmentation of Molecular Clouds and Star Formation*, Kluwer, Dordrecht, p.119
- Grauer R., Marliani C. 2000, *Phys. Rev. Lett.* 84, 4850
- Greaves J.S., White G.J., Williams P.G. 1992, *A&A* 257, 731
- Hartstein D., Liseau R. 1998, *A&A* 332, 703
- Hogerheijde M.R., van der Tak F.F.S. 2000, *A&A* 362, 697
- Juvela M. 1997, *A&A* 322, 943
- Juvela M., Padoan P. 1999, in Wootten A. (ed): *Science with the Atacama Large Millimeter Array*, ASP Conference Proceeding Vol. 235, p. 130
- Juvela M., Padoan P., Jimenez R. 2003, *ApJ* 591, 258
- Klein R.I., Fisher R.T., Krumholz M.R., McKee C.F. 2003, in *Winds, Bubbles, and Explosions: a conference to honor John Dyson*, Arthur S.J., Henney W.J. (eds), *Revista Mexicana de Astronomia y Astrofisica (Serie de Conferencias)* Vol. 15, p. 92
- Kunasz P., Auer L.H. 1988 *JSQRT* 39, 67

- Ossenkopf V. 2002, A&A 391, 295
- Padoan P., Juvela M., Bally J., Nordlund Å. 1998, ApJ 504, 300
- Padoan P., Juvela M., Bally J., Nordlund Å. 2000, ApJ 529, 259
- Padoan P., Goodman A., Juvela M. 2003, ApJ 588, 881
- Padoan P., Jimenez R., Juvela M., Nordlund Å. 2004, ApJ, 604, L49
- Pagani L. 1998, A&A 333, 269
- Park Y.-S., Hong S.S. 1995, A&A 300, 890
- Park Y.-S., Hong S.S., Minh Y.C. 1996, A&A 312, 981
- Rybicki G.B., Hummer D.G. 1991, A&A 245, 171
- Rybicki G.B., Hummer D.G. 1991, A&A 262, 209
- Scharmer G.B. 1981, ApJ 249, 720
- Snell R.L., Mundy L.G., Goldsmith P.F., Evans II N.J., Erickson N.R. 1984, ApJ 276, 625
- van Zadelhoff G.-J., Dullemond C.P., van der Tak F.F.S. et al. 2002, A&A 395, 373

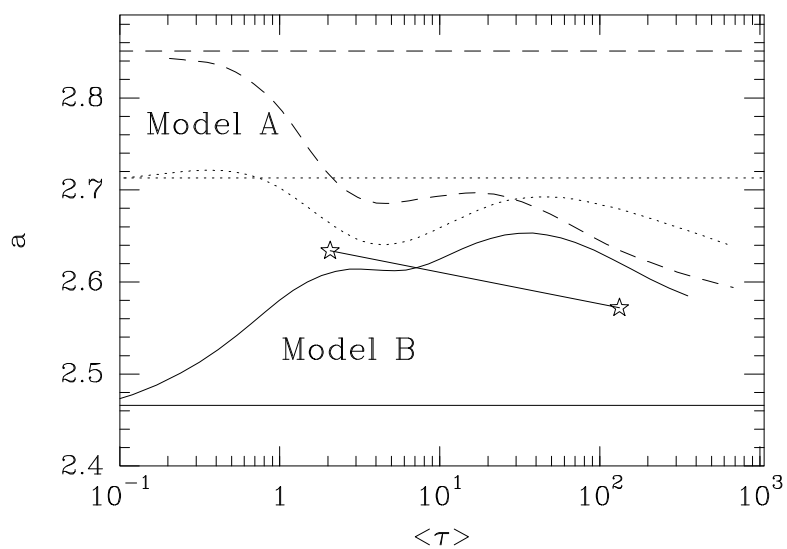


Fig. 14.— Slopes of the power spectra as a function of average optical depths. The curves show the behaviour for direction x in model B (solid line) and for model A in directions x (dashed line) and z (dotted line) according to LTE calculations with $T_{\text{ex}}=10$ K. The horizontal lines indicate the corresponding slopes for the column density maps. The stars show values for two non-LTE clouds ($T_{\text{kin}} = 10$ K) based on model B .